Supporting Information for

The Role of Surface Tension in the Crystallization of Metal Halide Perovskites

Ayan A. Zhumekenov,[†,⊥] *Victor M. Burlakov,*[§,⊥] *Makhsud I. Saidaminov,*[†,Δ] *Abdulilah Alofi,*[†] *Md Azimul Haque,*[‡] *Bekir Turedi,*[†] *Bambar Davaasuren,*[‡] *Ibrahim Dursun,*[†] *Namchul Cho,*[†,#] *Ahmed M. El-Zohry,*[†] *Michele De Bastiani,*[†] *Andrea Giugni,*[‡] *Bruno Torre,*[‡] *Enzo Di Fabrizio,*[‡] *Omar F. Mohammed,*[†] *Alexander Rothenberger,*[‡] *Tom Wu,*[‡] *Alain Goriely,*[§] *Osman M. Bakr*[†,*]

[†] King Abdullah University of Science and Technology (KAUST), KAUST Solar Center, Physical Sciences and Engineering Division (PSE), Thuwal 23955-6900, Saudi Arabia

[‡] King Abdullah University of Science and Technology (KAUST), Physical Sciences and Engineering Division (PSE), Thuwal 23955-6900, Saudi Arabia

[§] Mathematical Institute, University of Oxford, Woodstock Road, Oxford OX2 6GG, UK

[⊥] A.A.Z. and V.M.B. contributed equally to this work

Corresponding Author

*E-mail: osman.bakr@kaust.edu.sa

Contents

I. Materials and Methods

Materials. Methylammonium bromide and methylammonium iodide were purchased from Dyesol Limited (Australia). Lead bromide (≥ 98%), lead iodide (99.999% trace metal basis), DMF (anhydrous, 99.8%) and GBL (≥ 99%) were purchased from Sigma-Aldrich. Tin bromide (II) was purchased from Alfa Aesar (99.2%). All salts and solvents were used as received without any further purification. All syntheses were carried in 4 ml ChemGlass reaction vials of 33 expansion borosilicate glass corresponding to ASTM E-438 Type 1-Class A, USP Type 1 and ISO 3585.

For convenience, hereby we define molarity (M) as moles of solute per liter of solvent.

Growth of $MAPbI_3$ bulk single crystals with cuboid shape. A mixture of MAI (0.795 g, 5 mmol) and PbI_2 (1.153 g, 2.5 mmol) was dissolved in 2 ml GBL and filtered through 0.45 μm PTFE filter. 400 μL of the filtrate was transferred into a 4 ml vial, and the vial was placed on a hot plate at 60 °C. Then temperature was increased gradually to 96 °C when the formation of cuboid crystals was observed.

Growth of $MAPbBr_3$ PMFs. Solution A (1.5 M solution of MABr/$PbBr_2$ in DMF prepared at room temperature) and solution B (4.2 M solution of MABr/$PbBr_2$ in DMSO prepared at 60 °C) were mixed in different ratios (1:9, 2:8, 3:7, 4:6 and 5:5 by volume, respectively). 300 μL of each mixture was transferred into a 4 ml vial, and the vials were placed on a hot plate at 60 °C. Then the temperature was increased gradually to 90-100 °C when the formation of PMFs in "1:9" and "2:8" mixtures was observed. The crystals were extracted using a spatula and then dried on a filter paper. Note 1: Aluminum foil was used to cover the crystallization setup in order to avoid the temperature fluctuations and determine the threshold concentration more accurately. Note 2:

Opening vials to air decreases the crystallization onset temperature, since the air flow aids the removal of solvent vapor and also increases the solution surface tension.

Growth of $MAPbI_3$ PMFs. Solution C (2.5 M solution of 2MAI/PbI_2 in GBL prepared at room temperature) and solution D (4.5 M solution of 2MAI/PbI_2 in DMSO prepared at 70 °C) were mixed in 1:1 ratio by volume. 350 µL of the mixture was transferred into a 4 ml vial, and the vial was placed on a hot plate at 80 °C. Then the temperature was increased gradually to 100-110 °C when the formation of PMFs was observed. The crystals were extracted using a spatula and then dried on a filter paper.

Growth of $MASnBr_3$ PMFs. A mixture of MABr (1.12 g, 10 mmol) and $SnBr_2$ (2.79 g, 10 mmol) was dissolved in 2 ml of DMF, centrifuged at 7500 rpm for 5 minutes and filtered through 0.45 µm PTFE filter. 300 µL of the filtrate was transferred into a 4 ml vial, and the vial was placed on a hot plate at 40 °C. Then temperature was increased gradually to 60-70 °C when the formation of PMFs was observed. The crystals were extracted using a spatula and then dried on a filter paper.

Characterization. X-ray diffraction of as-prepared and ground crystals was performed on a Bruker AXS D8 Advance powder diffractometer using Cu-Kα radiation. Single crystal X-ray diffraction was carried out on a Stoe IPDS II diffractometer with Mo-Kα radiation at 298(2) K. High-resolution X-ray diffraction (Rocking Curve) was performed on a Bruker AXS D8 Advance DaVinci high-resolution diffractometer using Cu-Kα radiation. Scanning Electron Microscopy (SEM) images of PMFs were taken on a FEI Quanta 200F. The steady-state absorption was recorded using a Cary 6000i UV-Vis-NIR Spectrophotometer with an integrated sphere in absorbance mode. The steady-state photoluminescence was recorded using a Horiba JY LabRAM Aramis spectrometer with an Olympus lens; a 473 nm laser was used as the excitation source.

Pendant Drop and Contact Angle measurements were performed on a Kruss DSA25 drop shape analyzer. Temperature-dependent surface tension study was done using tempering chamber. The drop shape was analyzed on a Kruss Advance software.

Air plasma treatment. The glass surfaces of vials were treated for 5 min with high power air plasma generated by PDC-32G Harrick Plasma Cleaner.

Micro-Raman spectroscopy. Confocal Raman imaging was performed by excitation with a low intensity (~200 μW) linearly polarized laser (λ_0 = 633 nm) with f = 320 mm backscattering Raman spectrometer (Witec – AFM Raman spectrometer) equipped with EMCCD detector (Andor – Newton), 100X objective (0.9 NA – Zeiss), diffraction grating of 600 grooves/mm, and confocal collection fiber with a core of 100 μm. The effective spectral resolution was <9 cm^{-1}. A dichroic beam splitter rejects the laser line preventing the access to the spectral information below 80 cm^{-1}. An integration time was set at 2 s/pt.

Space-charge-limited current (SCLC) measurement. Gold electrodes of 100 nm thickness were deposited on both sides (sandwich configuration) of the $MAPbBr_3$ PMF by sputter deposition. The *I–V* characteristics of the prepared device was measured in the dark, under vacuum using a Keithley 2635A sourcemeter. The trap state density was estimated using a formula: $n_t = \frac{2V_{TFL}\varepsilon\varepsilon_0}{eL^2}$, where V_{TFL} is the trap-filled limit voltage, L is the thickness of the crystal, ε_0 is the vacuum permittivity, e is the electron charge, and ε is the dielectric constant taken as 25.5 for $MAPbBr_3$.

Photodetector Fabrication and Characterization. To fabricate the photodetector, 100 nm gold and 25 nm platinum were deposited on opposite faces of the 1 mm^2 sized $MAPbBr_3$ PMF. All photoresponse characteristics of the self-powered photodetector were measured on a probe station

connected to a Keithley 4200 semiconductor analyzer under dark and light conditions. To measure the white light and wavelength-dependent photoresponse, a calibrated LED kit by Metrohm Autolab system was used as the light source. An optical power meter was used to determine the power at different wavelengths. The responsivity (R) was calculated as $R = \Delta I/(PS)$, where ΔI is the difference between the photocurrent and the dark current, P is the incident power density, and S is the effective illuminated area. Detectivity was calculated using the equation $D = R/(2eJ_{dark})^{1/2}$, where J_{dark} is the dark current density. The response speed of the photodetector was measured using an Agilent MSO9104A oscilloscope with pulsed light excitation of 520 nm LED modulated by a function generator (Agilent 81150A).

II. Extended theoretical analysis

II.1. Free energy analysis

Consider the system of a unit volume containing solvent and A-molecules (the precursor). These molecules can be found in different forms. The A-molecules appear either as isolated molecules of the number concentration n_A, in nucleated particle containing n_p molecules, or inside complexes with the number concentration n_C. Therefore, the total concentration of A-molecules in the system is $m_{\mathrm{A}} = n_{\mathrm{A}} + n_{\mathrm{P}} + n_{\mathrm{C}}$. The solvent molecules can be found in the solution with the number concentration n_S or in complexes. Assuming that there are j solvent molecules in each complex, the total number of solvent molecules in the system is $m_{\mathrm{S}} = n_{\mathrm{S}} + j \cdot n_{\mathrm{C}}$.

The total free energy of the system containing one nucleated particle is

$$\begin{aligned} G = &-\varepsilon \cdot n_{\mathrm{P}} + \gamma \cdot S_{\mathrm{P}} - \varepsilon_A \cdot n_A - \varepsilon_{\mathrm{C}} \cdot n_{\mathrm{C}} - \varepsilon_{\mathrm{S}} \cdot n_{\mathrm{S}} + k_B T \cdot n_{\mathrm{C}} \cdot \ln\left(n_{\mathrm{C}} v_{\mathrm{C}}\right) + k_B T \cdot n_{\mathrm{A}} \cdot \ln\left(n_{\mathrm{A}} v_{\mathrm{A}}\right) \\ &+ k_B T \cdot n_{\mathrm{S}} \cdot \ln\left(n_{\mathrm{S}} v_{\mathrm{S}}\right) - k_B T \cdot \left(n_{\mathrm{A}} + n_{\mathrm{S}} + n_{\mathrm{C}}\right) \cdot \ln\left(n_{\mathrm{A}} v_{\mathrm{A}} + n_{\mathrm{S}} v_{\mathrm{S}} + n_{\mathrm{C}} v_{\mathrm{C}}\right) \end{aligned} \quad \text{(S1)}$$

where ε is the cohesive energy of A-molecules in the particle, $\varepsilon_A > 0$ and $\varepsilon_S > 0$ are the energies of A-molecule and solvent molecule, respectively, in the solution, $\varepsilon_C > 0$ is the binding energy of the complexes, S_P is the number of A-molecules on the surfaces of A-particle, T is the solution temperature, k_B is Boltzman's constant and v_S, v_C and v_A are the characteristic volumes of the solvent molecule, the complex, and the A-molecule, respectively.

Expressing n_S and n_A in terms of the total concentrations m_A and m_S, we rewrite eq (S1) in the form:

$$
\begin{aligned}
G = &-\varepsilon \cdot n_{\mathrm{P}} + \gamma \cdot S_{\mathrm{P}} - \varepsilon_A \cdot \left(m_{\mathrm{A}} - n_{\mathrm{P}} - n_{\mathrm{C}}\right) - \varepsilon_{\mathrm{C}} \cdot n_{\mathrm{C}} - \varepsilon_S \cdot \left(m_S - jn_C\right) + k_B T \cdot n_{\mathrm{C}} \cdot \ln\left(n_{\mathrm{C}} v_{\mathrm{C}}\right) \\
&+ k_B T \left(m_{\mathrm{A}} - n_{\mathrm{P}} - n_{\mathrm{C}}\right) \cdot \ln\left(\left(m_{\mathrm{A}} - n_{\mathrm{P}} - n_{\mathrm{C}}\right) v_{\mathrm{A}}\right) + k_B T \cdot \left(m_S - jn_C\right) \cdot \ln\left(\left(m_S - jn_C\right) v_{\mathrm{S}}\right) \\
&- k_B T \cdot \left(m_{\mathrm{A}} + m_S - jn_C - n_{\mathrm{P}}\right) \cdot \ln\left(\left(m_{\mathrm{A}} - n_{\mathrm{P}} - n_C\right) v_A + \left(m_S - jn_C\right) v_S + n_C v_C\right)
\end{aligned}
\tag{S2}
$$

We are interested in the equilibrium size of A-particle and equilibrium concentration n_C of the complexes in the solution. Therefore, we choose n_P and n_C as independent variables. The minimization of the free energy with respect to these two variables leads to the equations:

$$
\begin{aligned}
&\frac{\partial G}{\partial n_{\mathrm{P}}} = -\varepsilon + \varepsilon_A + \gamma \cdot \frac{2}{R_{cr}} - k_B T \cdot \ln\left(N_{\mathrm{A}}\right) = 0 \\
&\frac{\partial G}{\partial n_{\mathrm{C}}} = -\varepsilon_C + j\varepsilon_S + \varepsilon_A + k_B T \cdot \ln\left(N_{\mathrm{C}}\right) - k_B T \cdot \ln\left(N_{\mathrm{A}}\right) - jk_B T \cdot \ln\left(N_{\mathrm{S}}\right) = 0
\end{aligned}
\tag{S3}
$$

where R_{cr} is the particle critical radius and N_A, N_C and N_S are molar concentrations of corresponding species. These equations are very generic: the first one means an equivalence of molecular chemical potentials in the particle and in solution. The second equation shows that chemical potential of the complex is equal to the sum of the chemical potentials of the constituent molecules. Eqs (S3) hold in the bulk (volume) of the solution, near its surface, and at the interface with a substrate. Solving the first of eqs (S3) for the critical nucleus radius gives:

$$
R_{cr} = \frac{2\gamma}{\varepsilon - \varepsilon_A + k_B T \cdot \ln\left(N_{\mathrm{A}}\right)} \tag{S4}
$$

From the second of eqs (S3) we obtain the concentration of A–solvent complexes:

$$
N_C = N_A \cdot \left(N_S\right)^j \cdot \exp\left(\frac{\varepsilon_C - \varepsilon_A - j\varepsilon_S}{k_B T}\right) \tag{S5}
$$

Using this we can obtain equilibrium concentration N_A, which in case of $N_A << M_A$ and $\exp\left(\left(\varepsilon_C - \varepsilon_A - j\varepsilon_S\right)/k_BT\right) >> 1$ is approximated as

$$N_A \approx \frac{M_A}{\left(M_S\right)^j \cdot \left(1 - j^2 \frac{M_A}{M_S}\right)} \cdot \exp\left(-\frac{\varepsilon_C - \varepsilon_A - j\varepsilon_S}{k_BT}\right) \qquad \text{(S6)}$$

This expression illustrates the fact that the A-molecule concentration increases with increasing temperature, which is consistent with the inverse temperature crystallization concept.

Next step is to consider the conditions for A-particle nucleation in the solution. As we are interested in the onset of nucleation, i.e. in the situation when the first stable nucleus is about to form, it is reasonable to assume that the probability of such event is proportional to the concentration of critical clusters N_{crit}, i.e. the A-clusters with the critical radius R_{cr} given by eq (S4). This concentration can be estimated using eq (S5) as

$$N_{crit} = \left(N_A\right)^k \cdot \exp\left(-\frac{\Delta}{k_BT}\right) \qquad \text{(S7)}$$

where $k = \frac{4}{3}\pi R_{cr}^3$ and Δ is the nucleation barrier considered in the section below.

II.2. Nucleation

For illustration purposes we compare the nucleation barriers in the surface layer and the bulk of solution for the case of spherical nuclei. First of all we point out that the surface layer is very thin, just 2-3 intermolecular distances which amounts a fraction of the nanometer.[1] This suggests that the molar concentration of A-molecules in this layer is most likely the same as in the bulk. To

make such assertion consistent with eq (S6) we have to accept that the value of $E_C = \varepsilon_C - \varepsilon_A - j\varepsilon_S$ in the surface layer stays the same as in the bulk meaning that all the effects of surface tension in the surface layer are compensated for E_C. The nucleation barrier Δ is defined as the free energy required for transferring A-molecules from the solution to the particle of radius R_{cr}:

$$\Delta = \frac{4}{3}\pi R_{cr}{}^3 \cdot \left(-\varepsilon + \varepsilon_A - k_B T \cdot \ln N_A\right) + 4\pi\gamma R_{cr}{}^2 = \frac{16\pi}{3} \cdot \frac{\gamma^3}{\left(\varepsilon - \varepsilon_A + k_B T \cdot \ln\left(N_A\right)\right)^2} \qquad \text{(S8)}$$

Substituting here N_A from eq (S5) and using the conservation of $E_C = \varepsilon_C - \varepsilon_A - j\varepsilon_S$ gives:

$$\Delta \approx \frac{16\pi}{3}\gamma^3 \cdot \left(\varepsilon - E_C - \varepsilon_A + k_B T \cdot \ln\left(\frac{M_A}{\left(M_S\right)^j \cdot \left(1 - j^2 \frac{M_A}{M_S}\right)} \right) \right)^{-2} \qquad \text{(S9)}$$

As one can see from eq (S9), the nucleation barrier Δ depends on molar concentration of A-material, the difference between the cohesive energy of A-molecules in the particle ε and the sum of complex formation energy E_C and the energy of individual A-molecule in the solution ε_A. Note, that the energy of A-molecules in in the surface layer ε_{AS} must be different from that in the bulk ε_A. Indeed, the molecules in the surface layer experience tensile elastic stress, which accounts for surface tension. If elastic energy per A-molecule corresponding to this stress is ε_{surf} then the total energy of A-molecule in the surface layer should be

$$\varepsilon_{AS} = \varepsilon_A - \varepsilon_{surf} \qquad \text{(S10)}$$

indicating that the energy ε_{surf} decreases molecular binding energy in the surface layer. As a consequence the nucleation barrier in the surface layer Δ_S decreases compared to its bulk value:

$$\Delta_S \approx \frac{16\pi}{3}\gamma^3 \cdot \left(\varepsilon + \varepsilon_{surf} - E_C - \varepsilon_A + k_B T \cdot \ln\left(\frac{M_A}{\left(M_S\right)^j \cdot \left(1 - j^2 \frac{M_A}{M_S}\right)} \right) \right)^{-2} \qquad \text{(S11)}$$

if we recall that the A-molecules concentration in the surface layer is roughly the same as that in the bulk of the solution. From eqs (S9) and (S11) we see that $\Delta_S < \Delta$, which suggests that surface tension makes it easier for a particle to nucleate on the solution surface.

II.3. Growth

Here we want to argue that once nucleated the particle would grow anisotropically with the preferential lateral growth parallel to the solution surface. Indeed, as the surface layer is very thin the A-molecule supply to the growth front comes from the bulk. Therefore, the anisotropy of the growth rate can be only due to the rate of molecular integration to the particle structure. This rate can be treated within the Transition State Theory,[2] according to which the reaction rate is higher if the molecule in the initial state (solution) has higher chemical potential. The latter is true for A-molecules in the surface layer, which solvation energy $(-\varepsilon_{AS})$ is increased due to surface tension. As a result, the edge sides of a crystal are expected to grow faster than the bottom side (Figure S1A).

II.4. Floatation

Generally, the suspended object bends the liquid surface at its edges, forming an effective contact angle θ with the liquid (see Figure 1C).[3,4] The resultant surface tension force F_S acting on a solid object is tangential to the liquid surface at the contact point *O*. For illustrating the effect, consider a crystal plate of $a \times a \times h$ dimensions (see Figure 1C). Such a crystal of mass *m* and density ρ can be held on the solution surface by a combination of buoyant force and the surface tension force. The net force balance is as follows:

$$\rho_{sol} g a^2 H + 4a\sigma_{sol} \sin(\theta + \phi - 180^\circ) = mg \qquad \text{(S12)}$$

where ρ_{sol} and σ_{sol} are the solution density and surface tension coefficient, respectively, H is the distance between the meniscus and the bottom of the crystal plate, ϕ is the crystal wedge angle at the contact point, *g* is the gravitational constant (9.81 m/s^2). The eq (S12) can further be simplified by substituting $m = \rho a^2 h$, and assuming that $H \approx h$ and $\phi = 90^\circ$:

$$ah \approx \frac{4\sigma_{sol} \sin(\theta - 90^\circ)}{(\rho - \rho_{sol})g} \qquad \text{(S13)}$$

Here, the effective contact angle θ changes with the crystal plate mass and size ranging between the intrinsic contact angle θ_0 and $90^\circ + \theta_0$.[3,4] The equation clearly shows that the higher are the ρ_{sol}, σ_{sol} and θ_0 values, the larger crystal can be held on the solution surface.

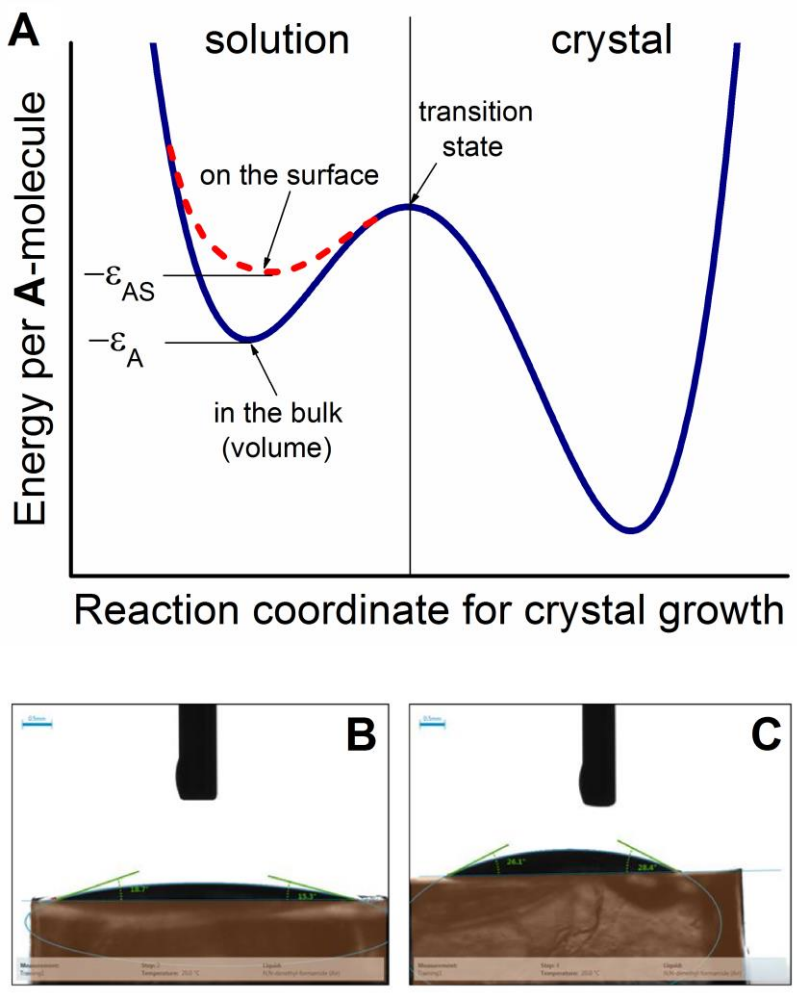

Figure S1. (A) Diagram illustrating the energy changes for the growth of a crystal from precursor **A**-molecules. Due to the effect of surface tension, the energy barrier for the integration of **A**-molecule to the nucleus/crystal structure is lower in the surface layer (red dashed line) compared to the bulk of a solution (blue line). This results in anisotropic lateral growth of a crystal.

Contact angle measurement between the $MAPbBr_3$ single crystal and the solution containing: (B) pure DMF solvent, (C) 1.5 M solution of $MABr/PbBr_2$ in DMF. Contact angle increases from ~15° (cosine = 0.966) for pure DMF to ~26° (cosine = 0.92) for 1.5 M solution.

III. Details of ST-ITC

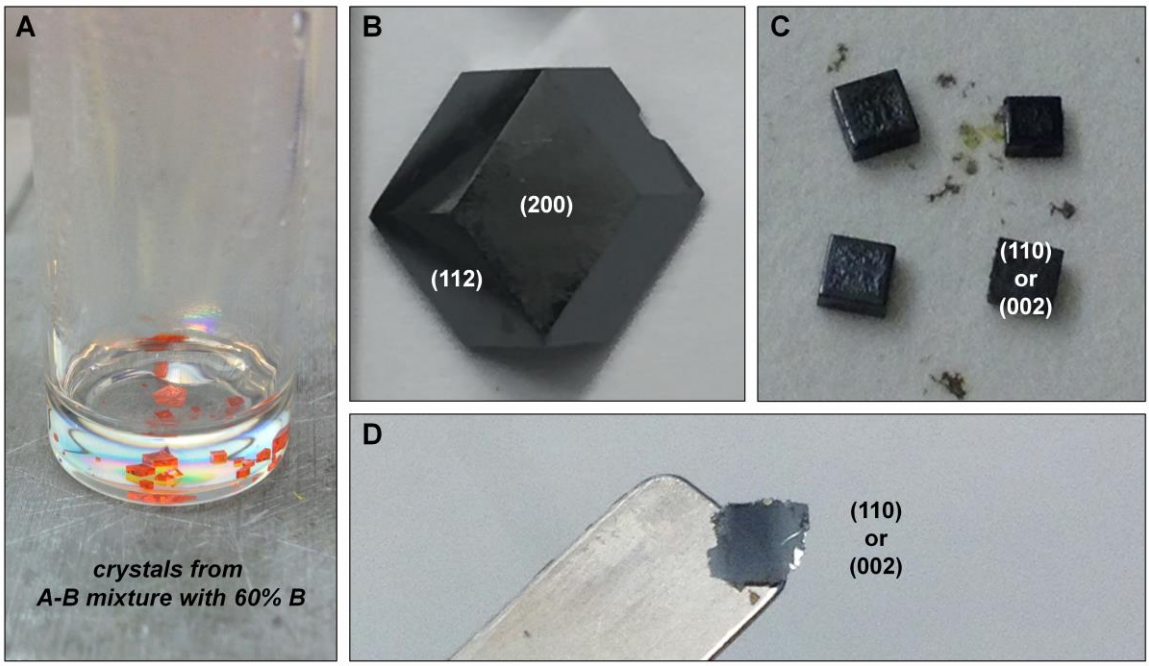

Figure S2. (A) A-B mixture with 60% of solution B results in mainly bulk crystals at the solution bottom and some irregularly shaped films on the solution surface. Photographs of $MAPbI_3$ bulk crystals with (B) dodecahedral and (C) cuboid shapes. The facets are indicated based on previous reports[5,6]. (D) Photograph of $MAPbI_3$ PMF. The facet is deduced from XRD.

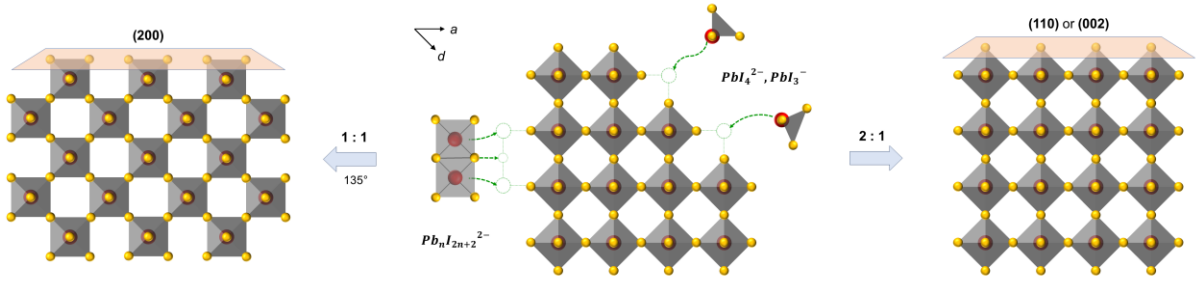

Figure S3. Growth mechanism of $MAPbI_3$ perovskite crystals from 1:1 (left) and 2:1 (right) molar ratio of MAI/PbI_2 precursors, resulting in (200) and (002)/(110) top facets, respectively.

IV. Crystallinity analysis

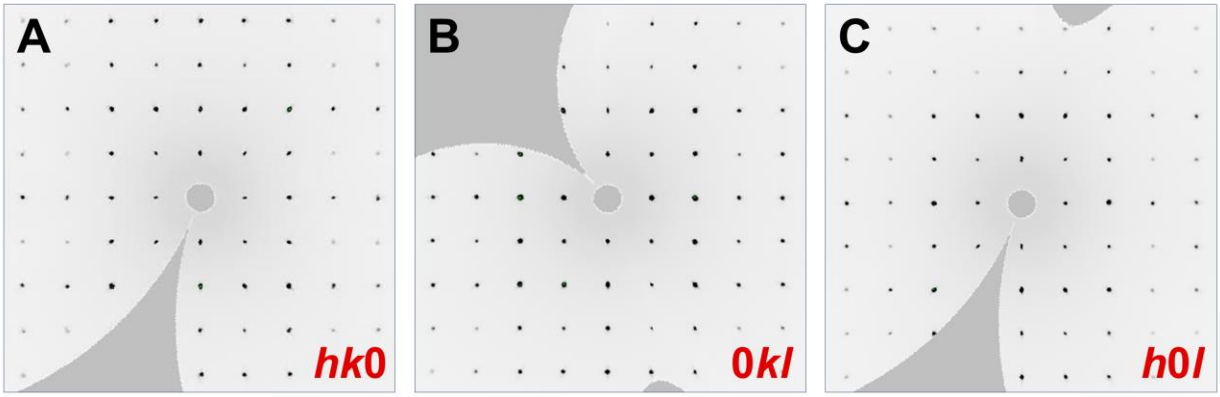

Figure S4. Single crystal X-ray diffraction analysis. The diffraction patterns of $MAPbBr_3$ PMF grown by ST-ITC method. The reconstructed Laue images of the (A) *hk*0, (B) 0*kl* and (C) *h*0*l* layers, clearly indicating the cubic symmetry and monocrystalline nature of the $MAPbBr_3$ PMF. Approximately 92% of the measured reflections was indexed to cubic unit cell with a = 5.9275(4) Å. No sign for the presence of other domains was observed.

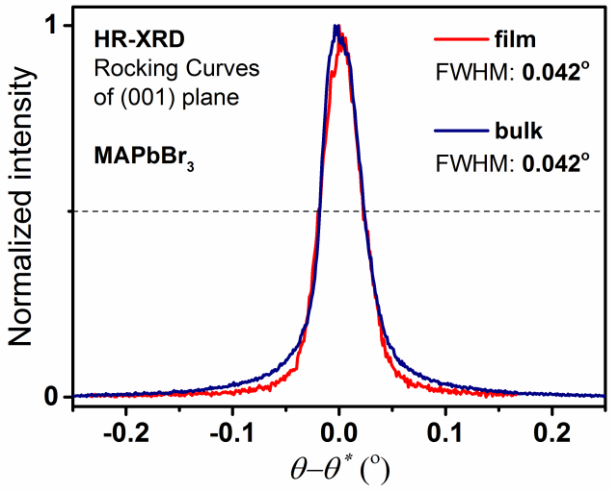

Figure S5. High-resolution X-ray diffraction analysis. Rocking Curve of the (001) diffraction plane of $MAPbBr_3$ PMF (film) showing a narrow peak with FWHM of 0.042°, on par with $MAPbBr_3$ bulk single crystal and other previous reports.[7,8]

V. Trap state density analysis

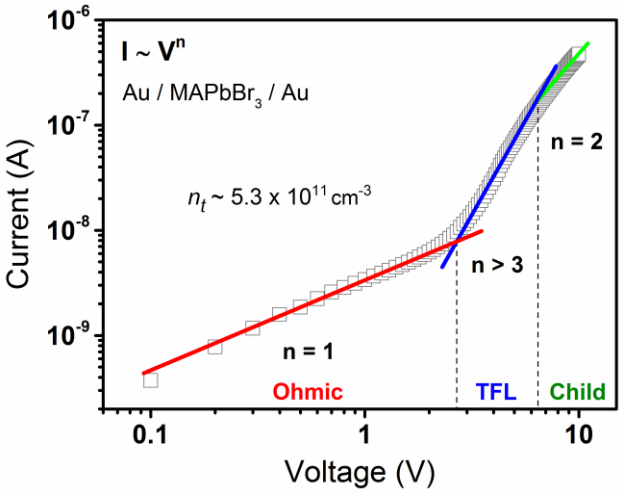

Figure S6. The SCLC measurement on $MAPbBr_3$ PMF. The *I–V* curve of the hole-only device (Au/$MAPbBr_3$ PMF/Au) measured in the dark. The trap state density of $MAPbBr_3$ PMF ($n_t \sim 5.3\times10^{11} cm^{-3}$) estimated from the plot is comparable to that of published perovskite single crystals (see Tables S1 and S6).

Table S1. Trap state density of $MAPbBr_3$ single crystals of different dimensions: monocrystalline films (PMF) possess slightly higher trap state density compared to bulk single crystals (SC), possibly due to their larger contact area with the solution per unit of crystal volume. (The solution can corrode the crystal surface and induce trap states).

Material	Trap state density (cm^{-3})	Contact-area-to-volume ratio (mm^{-1})
$MAPbBr_3$ PMF (this work)	5.3×10^{11}	~10^2–10^3
$MAPbBr_3$ PMF (ref. 7)	1.4×10^{11}	~10^2–10^3
$MAPbBr_3$ SC (ref. 9)	3.0×10^{10}	~2–3

VI. PL spectra correction

The PL spectra of $MAPbBr_3$ and $MAPbI_3$ PMFs were corrected based on previous reports[10,11] using the following equation, which considers the re-absorption of the emission:

$$I_{PL}^{cor} = I_{PL}^{obs}\left[\exp\left(\frac{\alpha^2 d^2}{4}\right)\mathrm{erfc}\left(\frac{\alpha d}{2}\right)\right]^{-1} \quad \text{(S14)}$$

where α is the absorption coefficient, and d is the carrier diffusion length. More detailed procedure will be given in the forthcoming publication.

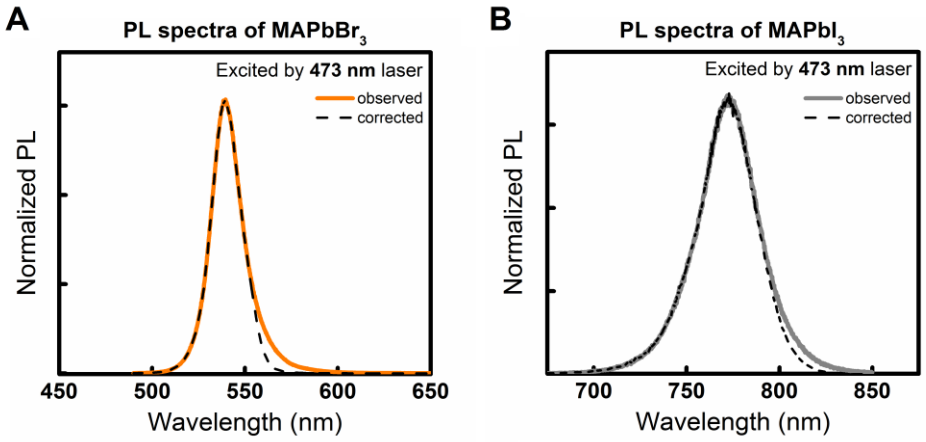

Figure S7. The observed and corrected PL spectra of (A) $MAPbBr_3$ and (B) $MAPbI_3$ PMFs.

VII. Experimental analysis of the effect of surface tension

VII.1. Concentration-dependent study of the solution surface tension

Table S2. Density and surface tension coefficients for **A**-**B** mixtures of different ratios at room temperature. The concentration here increases with the **B** content in **A**-**B** mixture.

A/B ratio (by volume)	density, ρ (g/ml)	σ_1	σ_2	σ_3	σ_4	σ_{ave} (mN/m)	St.Dev.
10 : 0	1.44	39.19	39.33	39.16	39.47	39.29	0.15
8 : 2	1.57	42.45	42.50	42.90	42.70	42.64	0.21
6 : 4	1.70	45.52	45.80	45.61	45.83	45.69	0.15
4 : 6	1.83	48.17	48.23	48.46	48.45	48.33	0.15
3 : 7	1.91	49.58	49.68	49.74	49.87	49.89	0.12
2 : 8	1.98	51.50	51.72	51.76	51.92	51.73	0.17
1 : 9	2.05	54.34	55.19	55.30	55.17	55.00	0.44
0 : 10	2.10	55.59	55.37	55.35	55.81	55.53	0.21

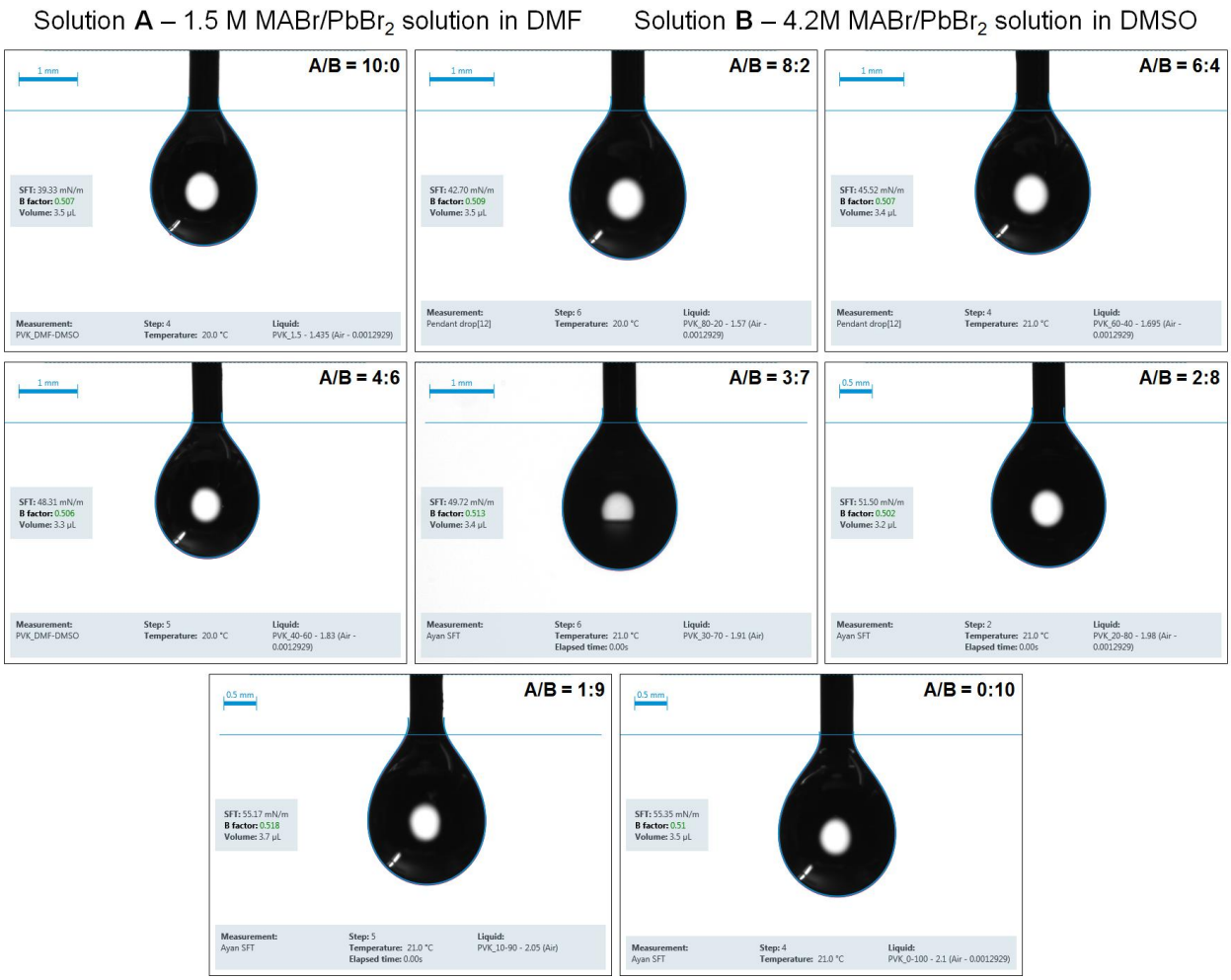

Figure S8. Pendant drop images corresponding to Table S2.

VII.2. Temperature-dependent study of the solution surface tension

Table S3. Surface tension coefficients measured at different temperatures for **A-B** mixtures of 2:8 and 3:7 ratios resulting in PMFs and bulk crystals, respectively.

Temp.	σ_1	σ_2	σ_3	σ_4	σ_{ave} **(mN/m)**	**St.Dev.**
2:8 mixture						
21 °C	51.50	51.72	51.76	51.92	51.73	0.17
30 °C	48.26	48.81	48.94	48.90	48.73	0.32
40 °C	46.98	46.83	47.12	46.86	46.95	0.13
50 °C	46.18	46.10	45.92	45.93	46.03	0.13
60 °C	45.56	45.32	45.24	45.18	45.33	0.17
70 °C	44.32	44.25	43.73	44.26	44.14	0.28
80 °C	42.95	42.95	43.26	43.12	43.07	0.15
3:7 mixture						
21 °C	49.58	49.68	49.74	49.87	49.72	0.12
30 °C	46.48	46.02	46.49	46.56	46.39	0.25
40 °C	45.01	45.34	45.26	45.53	45.28	0.22
50 °C	44.23	44.36	44.64	44.25	44.37	0.19
60 °C	43.42	43.45	43.33	44.02	43.55	0.31
70 °C	42.53	42.12	42.56	42.23	42.36	0.22
80 °C	41.17	41.05	41.46	40.90	41.14	0.24

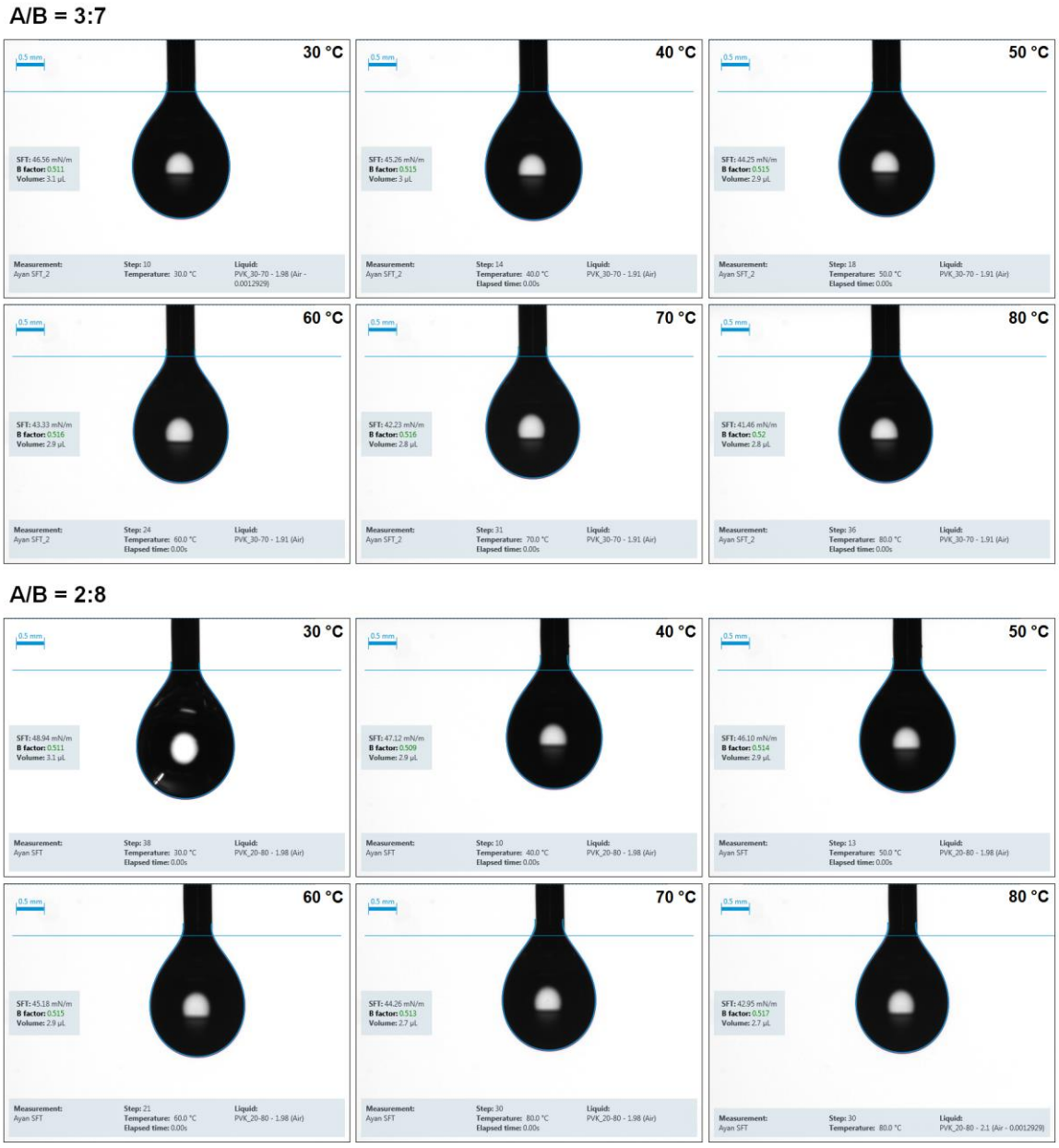

Figure S9. Pendant drop images corresponding to Table S3.

VII.3. Estimation of the vial surface energy

The Surface Energy of the vial glass was estimated using Owens-Wendt-Rabel-Kaelble (OWRK) method.[12-14] The OWRK method is based on measuring the contact angle (θ) between the studied solid and several liquids with known dispersive (σ_L^d) and polar (σ_L^p) components of surface tension coefficient.

The interfacial energy (σ_{SL}) between solid (***S***) and liquid (***L***) is described using the expression:[12]

$$\sigma_{SL} = \sigma_S + \sigma_L - 2\sqrt{\sigma_S^d \, \sigma_L^d} - 2\sqrt{\sigma_S^p \, \sigma_L^p} \qquad \text{(S15)}$$

where σ_S – surface energy of a solid, σ_L – surface tension of a liquid, d and p refer to dispersive and polar components of surface energy (or tension), respectively. Substituting this expression in the Young's equation[15] gives a linear function ($y = y_0 + kx$):

$$\frac{\sigma_L \, (cos\theta + 1)}{2\sqrt{\sigma_L^d}} = \sqrt{\sigma_S^p} \cdot \sqrt{\frac{\sigma_L^p}{\sigma_L^d}} + \sqrt{\sigma_S^d} \qquad \text{(S16)}$$

where $\frac{\sigma_L \, (cos\theta + 1)}{2\sqrt{\sigma_L^d}} = \boldsymbol{y}$, $\sqrt{\frac{\sigma_L^p}{\sigma_L^d}} = \boldsymbol{x}$, $\sqrt{\sigma_S^p} = \boldsymbol{k}$ and $\sqrt{\sigma_S^d} = \boldsymbol{y_0}$.

Obviously, at least two liquids are required to plot the function above. From the slope and y-intercept of the plotted line, the polar and dispersive components of solid's surface energy, respectively, can be calculated: $\sigma_S^p = k^2$ and $\sigma_S^d = {y_0}^2$.

To estimate the surface energy of the vial glass (**S**) without and after plasma treatment, we used the following liquids (**L**): water, ethylene glycol (EG), dimethyl sulfoxide (DMSO) and diiodo-methane (DIM). The results are summarized below.

Table S4. Contact angles between the liquids with known polar and dispersive components of surface tension and the vial glass (A) without and (B) after its plasma treatment.

Solvent (L)	**Surface Tension (mN/m)**			**Contact angle, θ (°)**	x	y	k	y_0
	Total, σ^{tot}	Disperse, σ^{d}	Polar, σ^{p}					
(A) without plasma treatment								
Water[16,17]	72.80	21.80	51.00	75.17	1.53	9.79	3.14	4.87
EG[16]	48.20	18.90	29.30	55.22	1.25	8.71		
DMSO[18]	42.80	27.00	15.80	42.50	0.76	7.15		
DIM[19]	50.80	49.00	1.80	57.88	0.19	5.56		
(B) after plasma treatment								
Water[16,17]	72.80	21.80	51.00	12.25	1.53	15.41	7.13	4.51
DIM[19]	50.80	49.00	1.80	51.80	0.19	5.87		

The surface energy of the borosilicate glass (vial) **without** plasma treatment:

polar component: $\sigma_{vial}^{p} = 9.9$ mN/m

dispersive component: $\sigma_{vial}^{d} = 23.7$ mN/m

total: $\sigma_{vial} = 33.6$ mN/m

The surface energy of the borosilicate glass (vial) **after** plasma treatment:

polar component: $\sigma_{vial*}^{p} = 50.9$ mN/m

dispersive component: $\sigma_{vial*}^{d} = 20.3$ mN/m

total: $\sigma_{vial*} = 71.2$ mN/m

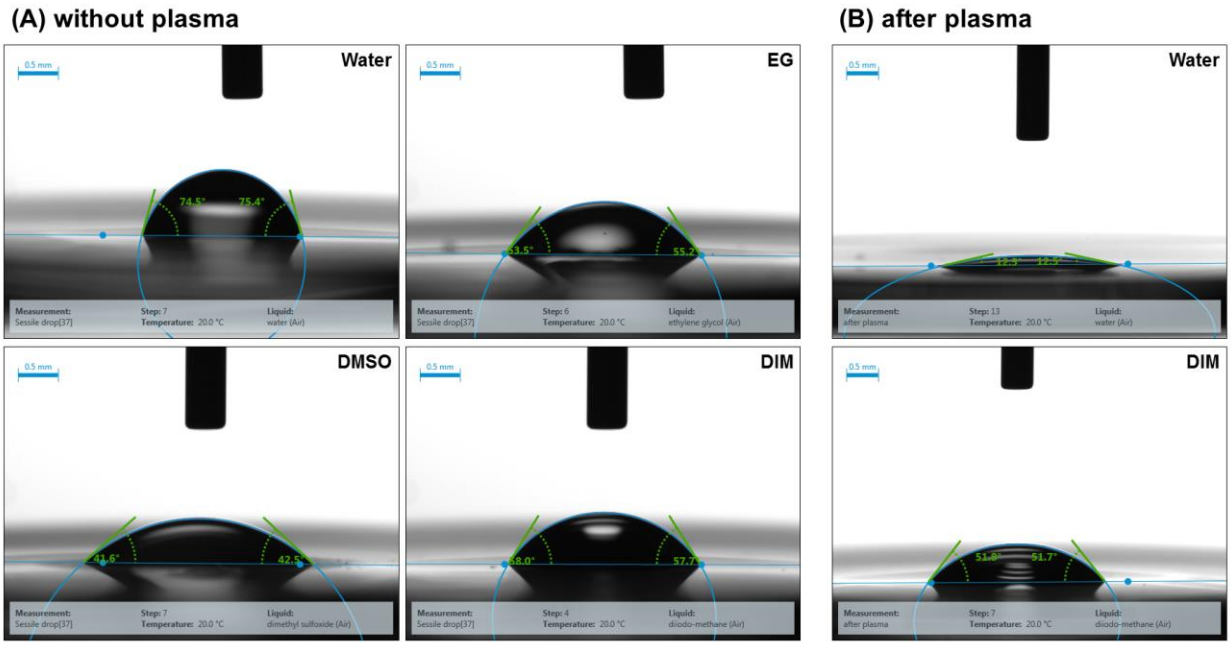

Figure S10. Contact angle images corresponding to Table S4.

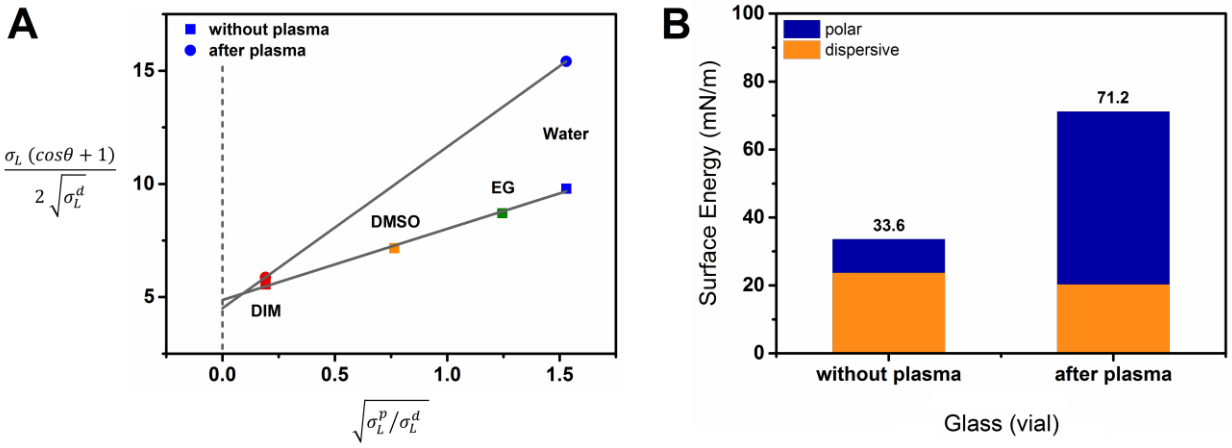

Figure S11. (A) The OWRK plots for the surface energy of the vial glass without (squares) and after (circles) plasma treatment. Each point reflects the interaction between the glass and the specified liquid. (B) Surface energy of the glass (with polar and dispersive components) wihtout and after plasma treatment.

VII.4. Estimation of the solution-vial interface energy

Here, the interface energies ($\sigma_{sol-vial}$) between the perovskite solutions (***sol***) and the glass (***vial***) are calculated using the Young's equation[15] from the surface energy of a glass (σ_{vial}), the surface tension of a solution (σ_{sol}) and the contact angle between two phases (θ):

$$cos\theta = \frac{\sigma_{vial} - \sigma_{sol-vial}}{\sigma_{sol}} \quad \text{(S17)}$$

Table S5. Solution–vial interface energies for pure solution **A**.

σ_{sol} (mN/m)	Plasma treatment	σ_{vial} (mN/m)	Contact angle, θ (°)	$cos\theta$	$\sigma_{sol-vial}$ (mN/m)
39.29	No	33.60	42.80	0.734	4.77
39.29	Yes	71.20	< 10	~ 1	~ 31.90

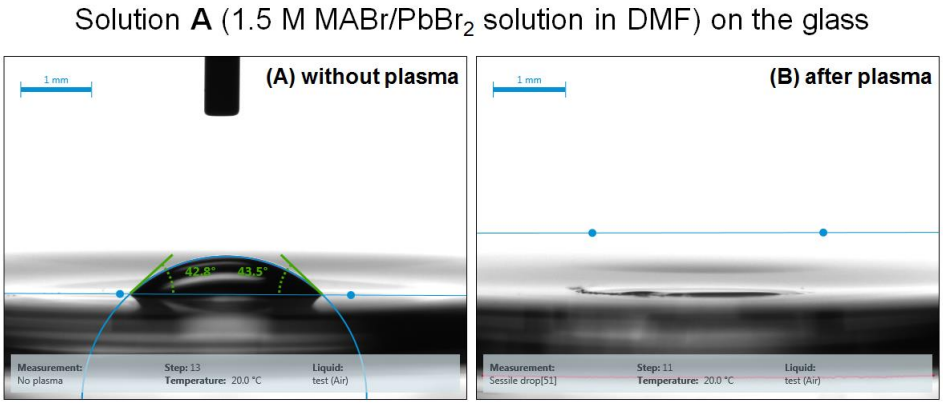

Figure S12. Contact angle images of 1.5 M MABr/$PbBr_2$ on the glass (A) without and (B) after plasma treatment.

VIII. Raman study of $MAPbBr_3$ PMF

Micro-Raman scattering is an optical technique that inherently reports structural information about the surface layer of an optically opaque sample, or in case of a transparent sample the near-surface layer (~1 μm in depth). In our specific case, considering that λ_0 ~2 eV is below the band gap of the $MAPbBr_3$ (~2.2 eV) and the absorbance at λ_0 is <0.1, the collected measurements allow to evaluate the vibrational near-surface properties of the material.

Figure S13 shows the characteristic Raman spectrum of the sample. The richness of peaks reflects the complex structure of the fundamental unit cell of the crystal. The spectrum can be subdivided in distinct regions: the internal vibrations of the $PbBr_3$ network (<150 cm^{-1}), the MA^+ cation librations (140−180 cm^{-1}), and the internal vibrations of the MA^+ cations (800−3100 cm^{-1}). The peak at 326 cm^{-1} correspond to the restricted rotation modes of MA^+ embedded in $MAPbBr_3$. In particular, $MAPbBr_3$ low frequency peaks are typical for crystals with cubic symmetry, expected to have no Raman-active phonon modes, i.e. the $MAPbBr_3$ crystal exhibits Raman spectrum with broad peaks with respect to the other perovskites characterized by lowered orthorhombic, tetragonal or trigonal symmetry.

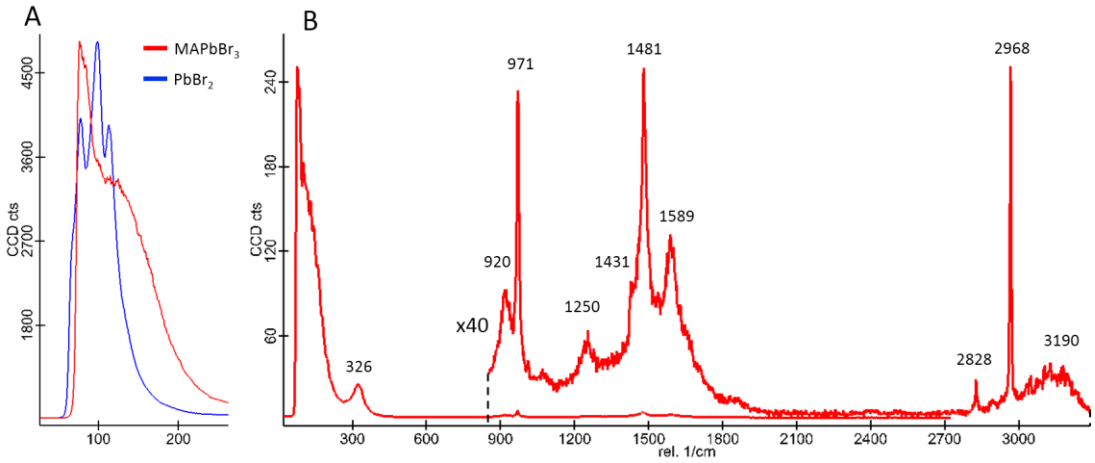

Figure S13. (A) Low frequency Raman spectra comparison between $MAPbBr_3$ PMF and $PbBr_2$ precursor. (B) Measured Raman spectra of $MAPbBr_3$ PMF.

It is noteworthy that the Raman signal in the region of 50−250 cm^{-1} that refers to the modes of the $PbBr_3$ is by far the most intense portion of the spectrum (Figure S13B). By comparing this region to the spectrum of lead bromide ($PbBr_2$) – the degradation product of $MAPbBr_3$ perovskite – the quality of the sample against contamination, structural defects and/or precursor residues in the crystal can be evaluated. As seen from Figure S13A, the Raman spectrum of $PbBr_2$ consists of several bands which clearly differ from the Raman spectrum of $MAPbBr_3$ PMF. Thus, we can conclude that no residual $PbBr_2$ presents in $MAPbBr_3$ PMFs.

Following the literature assignations,[20] the sharp and intense bands at 971 and 1481 cm^{-1} are attributed to the C-N stretching and the NH_3^+ asymmetric bending modes, respectively, while the signal at 1431 cm^{-1} – to the NH_3^+ symmetric bending modes, and the signals at 920 and 1250 cm^{-1} – to the rocking modes of MA^+. The peak at 1589 cm^{-1} is assigned to the twisting mode of NH_3^+. The high frequency peaks at 2828 cm^{-1} and 2968 cm^{-1} correspond to the N^+-H stretching and the CH_3 asymmetric stretching, respectively. The band at 3190 cm^{-1} is constituted of the splitting of the NH_3^+ symmetric stretching.

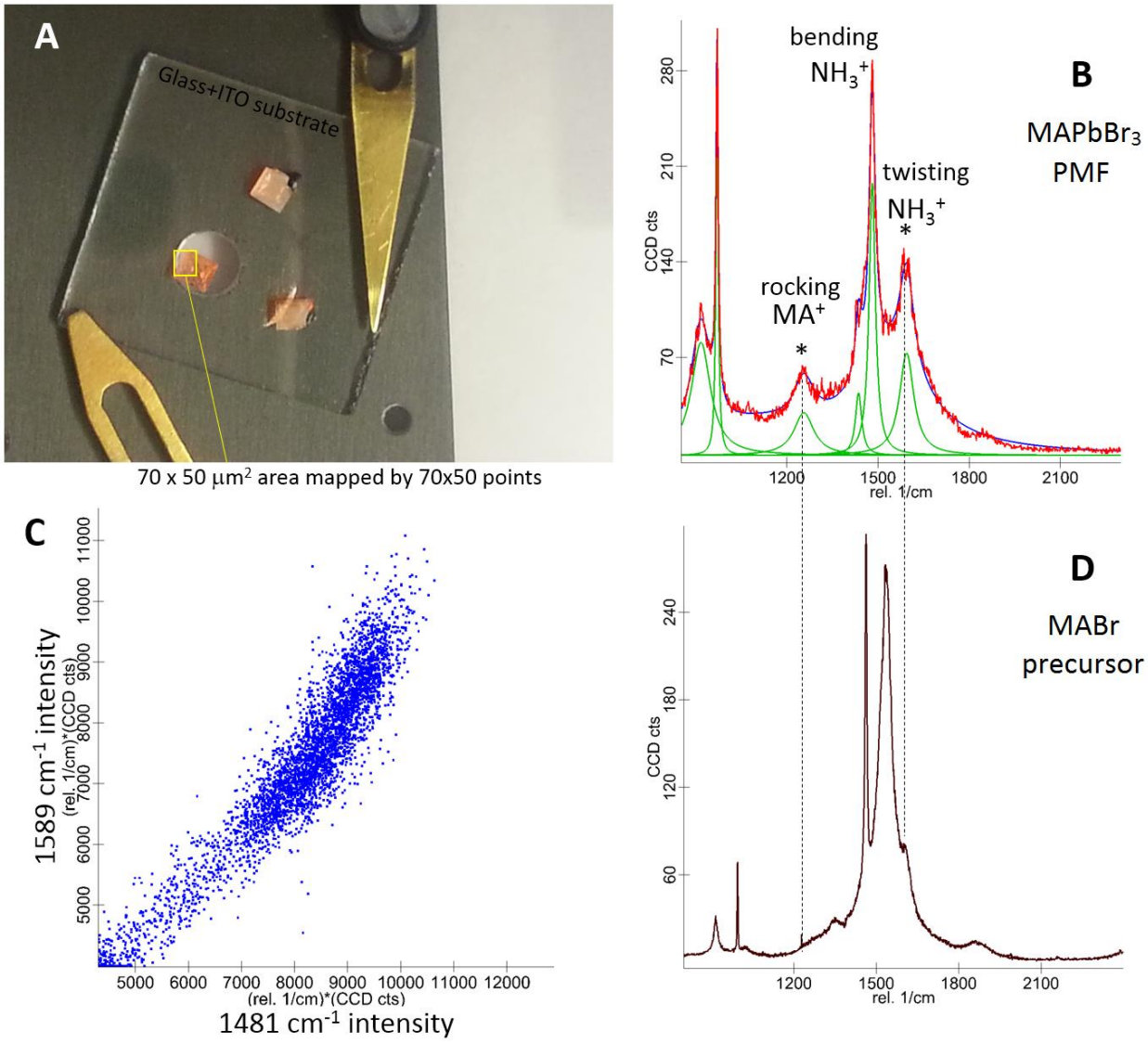

Figure S14. (A) Photograph of $MAPbBr_3$ PMFs used for investigation by the Raman imaging spectroscopy as described in the text. (B) Representative spectrum (red) superimposed with the fitted model (blue) constituted of Lorentzian curves (green). Peaks considered in the discussion are indicated. (C) Correlation graph between 1481 and 1589 cm^{-1} peak intensities, demonstrating with a linear correlation the chemical/structural homogeneity at microscale. (D) Raman spectrum of MABr powder.

To demonstrate the structural homogeneity of $MAPbBr_3$ PMF, we briefly discuss the results of one of the Raman imaging analysis performed. A 70x50 μm^2 area of the $MAPbBr_3$ PMF was mapped by 70x50 Raman points (Figure S14A), each point representing a single spectrum from 80 to 3400 cm^{-1}. In Figure S14B, we show 800–2400 cm^{-1} spectral region of one of the Raman points. The spectrum is constituted of seven Lorentzian shape functions; this allowed the evaluation of all the significant parameters: peak position, width, and integrated area under the curves. For each parameter, we have then reconstructed the intensity map and obtained the corresponding statistical distribution, as shown in Figure S15A–S15B for the peak at 1481 cm^{-1} and in Figure S15C–S15D for the peak at 1589 cm^{-1}. Comparing the reference spectrum of MABr (Figure S14D) to the one of $MAPbBr_3$ (Figure S14B), we observed that the MA^+ rocking mode (1248 cm^{-1}) and the twisting mode (1589 cm^{-1}) of the NH_3^+ clearly measurable in the PMF, barely arise in MABr, implying that these modes are highly sensitive to the environment. This fact also indicates that the chemical interactions between the inorganic framework and the organic cation takes places through the NH_3^+. Considered that, the correlation graph between two spectral components that have different sensitivity to the microenvironment should allow to quantify the homogeneity and structural quality of the sample by adopting one component, arbitrarily chosen, as an internal reference of the spectrum. As example, we report in Figure S14C the correlation graph between the integrated area under the curves of the 1481 cm^{-1} and 1589 cm^{-1} peaks. It shows almost linear relation indicating a high quality of the crystal at chemical/structural level. The appreciable intensity variations are essentially due to optical effects and thermal fluctuations of the instrument during the measurement.

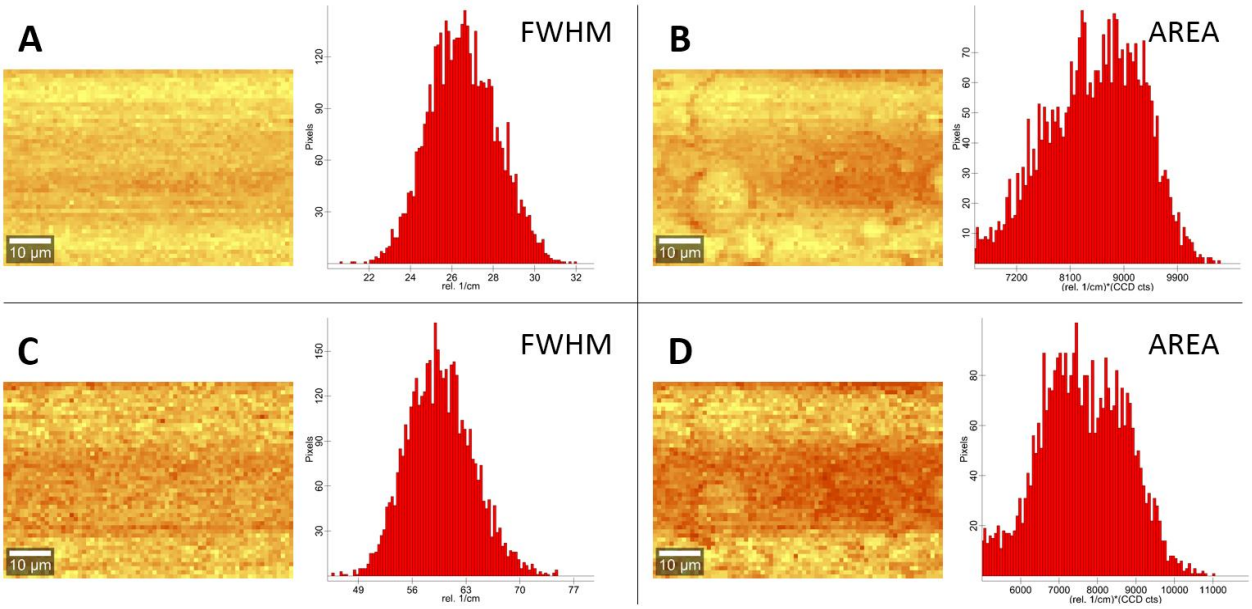

Figure S15. Raman imaging analysis results for 70x50 µm^2 area of $MAPbBr_3$ PMF. On the left panels: the FWHM and the integrated area under the fitted curves corresponding to the bending of NH_3^+ at 1481 cm^{-1} (A and B, respectively) and twisting of NH_3^+ at 1589 cm^{-1} (C and D, respectively). On the right panels: the corresponding statistical distribution of the recorded values.

IX. Characteristics of the self-powered Schottky photodetector based on $MAPbBr_3$ PMF

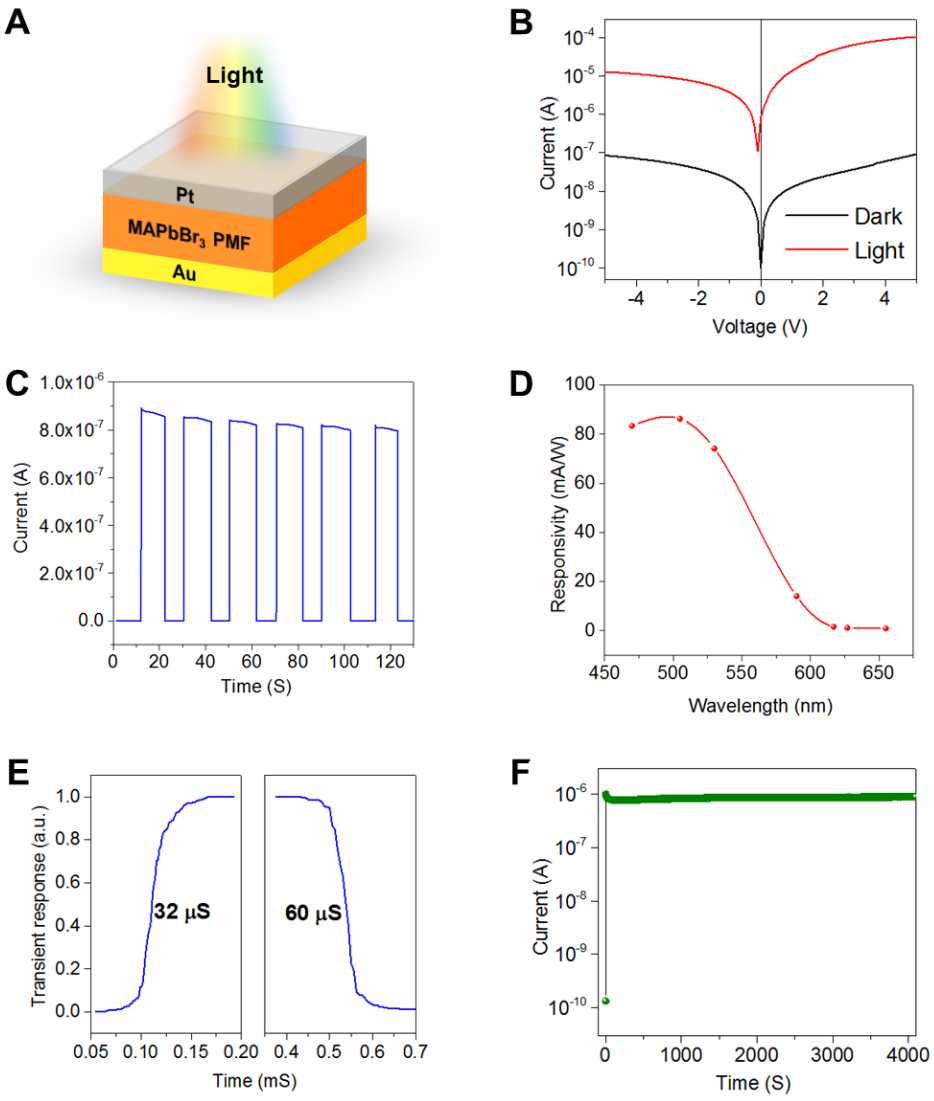

Figure S16. Device Characteristics. (A) Schematic architecture of the photodetector based on $MAPbBr_3$ PMF. (B) Dark and light (1 mW/cm^2) *I–V* curves. (C) Photoresponse under light pulses measured at zero-bias. (D) Responsivity as a function of wavelength. (E) Transient response at zero-bias showing a rise time of 32 µs and a decay time of 60 µs. (F) Current stability measured under continuous illumination.

X. Comparison of the state-of-the-art perovskite photodetectors based on single crystals

Table S6. The device performance of the state-of-the-art perovskite photodetectors with respect to the trap state density of the corresponding perovskite single crystals used for their fabrication.

Material	Traps (cm^{-3})	Device architecture	Operation mode	used light (mW/cm^2)	R (mA/W)	D (Jones)
$MAPbBr_3$ (this work)	5.3×10^{11}	vertical Pt/SC (15 μm)/Au	self-powered (at 0 V)	1	87	1×10^{12}
$MAPbBr_3$ (ref. 21)	10^9–10^{10}	vertical Pt/SC (150 μm)/Au	self-powered (at 0 V)	100	2	1.4×10^{10}
$MAPbBr_3$ (ref. 22)	–	vertical Ga/SC (~1 mm)/Au	under bias (at -4 V)	0.4	–	2×10^{10}
$CsPbBr_3$ (ref. 23)	4.2×10^{10}	vertical Pt/SC (~1 mm)/Au	self-powered (at 0 V)	10	28	1.7×10^{11}
$MAPbI_3$ (ref. 24)	–	lateral Al/SC/Au	self-powered (at 0 V)	1	~0.5	–
$MAPbI_3$ (ref. 5,25)	10^8–10^9	lateral Au/SC/Au	under bias (at 1–2 V)	0.9 [25] 1 [5]	1500 [25] 2550 [5]	–
$FAPbI_3$ (ref. 26)	1.3×10^{10}	lateral Au/SC/Au	under bias (at 8 V)	1	~1800	–
$MAPbCl_3$ (ref. 27)	3.1×10^{10}	vertical Pt/SC (350 μm) /Ti/Au	under bias (at 15 V)	1000	47	1.2×10^{10}

(SC – single crystal, R – responsivity, D – detectivity).

References

(1) Marchand, A.; Weijs, J. H.; Snoeijer, J. H.; Andreotti, B. Why Is Surface Tension a Force Parallel to the Interface? *Am. J. Phys.* **2011**, *79*, 999-1008.

(2) Laidler, K. J.; King, M. C. Development of Transition-State Theory. *J. Phys. Chem.* **1983**, *87*, 2657-2664.

(3) Oliver, J. F.; Huh, C.; Mason, S. G. Resistance to Spreading of Liquids by Sharp Edges. *J. Colloid Interface Sci.* **1977**, *59*, 568-581.

(4) Singh, P.; Joseph, D. D. Fluid Dynamics of Floating Particles. *J. Fluid Mech.* **2005**, *530*, 31-80.

(5) Lian, Z.; Yan, Q.; Lv, Q.; Wang, Y.; Liu, L.; Zhang, L.; Pan, S.; Li, Q.; Wang, L.; Sun, J.-L. High-Performance Planar-Type Photodetector on (100) Facet of $MAPbI_3$ Single Crystal. *Sci. Rep.* **2015**, *5*, 16563.

(6) Zhang, Y.; Huang, F.; Mi, Q. Preferential Facet Growth of Methylammonium Lead Halide Single Crystals Promoted by Halide Coordination. *Chem. Lett.* **2016**, *45*, 1030-1032.

(7) Peng, W.; Wang, L.; Murali, B.; Ho, K.-T.; Bera, A.; Cho, N.; Kang, C.-F.; Burlakov, V. M.; Pan, J.; Sinatra, L. *et al.* Solution-Grown Monocrystalline Hybrid Perovskite Films for Hole-Transporter-Free Solar Cells. *Adv. Mater.* **2016**, *28*, 3383-3390.

(8) Zhumekenov, A. A.; Saidaminov, M. I.; Haque, M. A.; Alarousu, E.; Sarmah, S. P.; Murali, B.; Dursun, I.; Miao, X.-H.; Abdelhady, A. L.; Wu, T. et al. Formamidinium Lead Halide Perovskite Crystals with Unprecedented Long Carrier Dynamics and Diffusion Length. *ACS Energy Lett.* **2016**, *1*, 32-37.

(9) Saidaminov, M. I.; Abdelhady, A. L.; Murali, B.; Alarousu, E.; Burlakov, V. M.; Peng, W.; Dursun, I.; Wang, L.; He, Y.; Maculan, G. et al. High-Quality Bulk Hybrid Perovskite Single Crystals within Minutes by Inverse Temperature Crystallization. *Nat. Commun.* **2015**, *6*, 7586.

(10) Murali, B.; Dey, S.; Abdelhady, A. L.; Peng, W.; Alarousu, E.; Kirmani, A. R.; Cho, N.; Sarmah, S. P.; Parida, M. R.; Saidaminov, M. I. *et al.* Surface Restructuring of Hybrid Perovskite Crystals. *ACS Energy Lett.* **2016**, *1*, 1119-1126.

(11) Niesner, D.; Schuster, O.; Wilhelm, M.; Levchuk, I.; Osvet, A.; Shrestha, S.; Batentschuk, M.; Brabec, C.; Fauster, T. Temperature-Dependent Optical Spectra of Single-Crystal $(CH_3NH_3)PbBr_3$ Cleaved in Ultrahigh Vacuum. *Phys. Rev. B* **2017**, *95*, 075207.

(12) Owens, D. K.; Wendt, R. C. Estimation of the Surface Free Energy of Polymers. *J. Appl. Polym. Sci.* **1969**, *13*, 1741-1747.

(13) Rabel, W. Einige Aspekte Der Benetzungstheorie Und Ihre Anwendung Auf Die Untersuchung Und Veränderung Der Oberflächeneigenschaften Von Polymeren. *Farbe Lack* **1971**, *77*, 997-1006.

(14) Kaelble, D. H. Dispersion-Polar Surface Tension Properties of Organic Solids. *J. Adhes.* **1970**, *2*, 66-81.

(15) Young, T. An Essay on the Cohesion of Fluids. *Philos. Trans. R. Soc. London* **1805**, *95*, 65-87.

(16) Jańczuk, B.; Białopiotrowicz, T.; Wójcik, W. The Components of Surface Tension of Liquids and Their Usefulness in Determinations of Surface Free Energy of Solids. *J. Colloid Interface Sci.* **1989**, *127*, 59-66.

(17) Jańczuk, B.; Białlopiotrowicz, T. Surface Free-Energy Components of Liquids and Low Energy Solids and Contact Angles. *J. Colloid Interface Sci.* **1989**, *127*, 189-204.

(18) Koenhen, D. M.; Smolders, C. A. The Determination of Solubility Parameters of Solvents and Polymers by Means of Correlations with Other Physical Quantities. *J. Appl. Polym. Sci.* **1975**, *19*, 1163-1179.
(19) Fernández, V.; Khayet, M. Evaluation of the Surface Free Energy of Plant Surfaces: Toward Standardizing the Procedure. *Front. Plant Sci.* **2015**, *6*, 510.
(20) Xie, L.-Q.; Zhang, T.-Y.; Chen, L.; Guo, N.; Wang, Y.; Liu, G.-K.; Wang, J.-R.; Zhou, J.-Z.; Yan, J.-W.; Zhao, Y.-X. *et al.* Organic-Inorganic Interactions of Single Crystalline Organolead Halide Perovskites Studied by Raman Spectroscopy. *Phys. Chem. Chem. Phys.* **2016**, *18*, 18112-18118.
(21) Shaikh, P. A.; Shi, D.; Retamal, J. R. D.; Sheikh, A. D.; Haque, M. A.; Kang, C.-F.; He, J.-H.; Bakr, O. M.; Wu, T. Schottky Junctions on Perovskite Single Crystals: Light-Modulated Dielectric Constant and Self-Biased Photodetection. *J. Mater. Chem. C* **2016**, *4*, 8304-8312.
(22) Fang, Y.; Dong, Q.; Shao, Y.; Yuan, Y.; Huang, J. Highly Narrowband Perovskite Single-Crystal Photodetectors Enabled by Surface-Charge Recombination. *Nat. Photonics* **2015**, *9*, 679-686.
(23) Saidaminov, M. I.; Haque, M. A.; Almutlaq, J.; Sarmah, S.; Miao, X.-H.; Begum, R.; Zhumekenov, A. A.; Dursun, I.; Cho, N.; Murali, B. *et al.* Inorganic Lead Halide Perovskite Single Crystals: Phase-Selective Low-Temperature Growth, Carrier Transport Properties, and Self-Powered Photodetection. *Adv. Opt. Mater.* **2017**, *5*, 1600704.
(24) Ding, J.; Fang, H.; Lian, Z.; Li, J.; Lv, Q.; Wang, L.; Sun, J.-L.; Yan, Q. A Self-Powered Photodetector Based on a $CH_3NH_3PbI_3$ Single Crystal with Asymmetric Electrodes. *CrystEngComm* **2016**, *18*, 4405-4411.
(25) Liu, Y.; Zhang, Y.; Yang, Z.; Yang, D.; Ren, X.; Pang, L.; Liu, S. Thinness- and Shape-Controlled Growth for Ultrathin Single-Crystalline Perovskite Wafers for Mass Production of Superior Photoelectronic Devices. *Adv. Mater.* **2016**, *28*, 9204-9209.
(26) Liu, Y.; Sun, J.; Yang, Z.; Yang, D.; Ren, X.; Xu, H.; Yang, Z.; Liu, S. 20-mm-Large Single-Crystalline Formamidinium-Perovskite Wafer for Mass Production of Integrated Photodetectors. *Adv. Opt. Mater.* **2016**, *4*, 1829-1837.
(27) Maculan, G.; Sheikh, A. D.; Abdelhady, A. L.; Saidaminov, M. I.; Haque, M. A.; Murali, B.; Alarousu, E.; Mohammed, O. F.; Wu, T.; Bakr, O. M. $CH_3NH_3PbCl_3$ Single Crystals: Inverse Temperature Crystallization and Visible-Blind UV-Photodetector. *J. Phys. Chem. Lett.* **2015**, *6*, 3781-3786.